

Quantum theory of superresolution for two incoherent optical point sources

Mankei Tsang,^{1,2,*} Ranjith Nair,¹ and Xiao-Ming Lu¹

¹*Department of Electrical and Computer Engineering,*

National University of Singapore, 4 Engineering Drive 3, Singapore 117583

²*Department of Physics, National University of Singapore, 2 Science Drive 3, Singapore 117551*

(Dated: July 2, 2022)

Rayleigh's criterion for resolving two incoherent point sources has been the most influential measure of farfield optical imaging resolution for over a century. In the context of statistical image processing, violation of the criterion is especially detrimental to the estimation of the separation between the sources, and modern superresolution techniques rely on suppressing the emission of close sources to enhance the localization precision. Using quantum optics, quantum information theory, and statistical analysis, here we show that, even if two close incoherent sources emit simultaneously, measurements with linear optics and photon counting can estimate their separation almost as precisely as conventional methods do for isolated sources, rendering Rayleigh's criterion irrelevant to the problem. Our results demonstrate that superresolution can be achieved not only for fluorophores but also for stars.

Rayleigh's criterion for resolving two incoherent point sources, requiring them to be separated at least by a diffraction-limited spot size on the image plane [1], has been the most influential measure of optical imaging resolution for over a century. More recently, insights from quantum optics [2] and statistics [3] have led to revolutions in farfield superresolution techniques [4–6] beyond his criterion. The techniques proposed in Refs. [2, 3] rely on locating a point source when no other nearby sources are radiating in the same optical mode. While such techniques have achieved spectacular success in microscopy, they require sophisticated control of the emission of special fluorophores and are irrelevant to astronomy and remote sensing.

For two sources with overlapping radiations on the image plane, studies [7, 8] have found that signal processing of the imaging data can still determine their locations, although the precision in the presence of photon shot noise quickly deteriorates when Rayleigh's criterion is violated. The precision degradation is mandated by the Cramér-Rao lower error bound [9], suggesting that the degradation is fundamental to direct imaging. Given such prior work, conventional wisdom thus suggests that the positions of two incoherent sources should become harder to estimate when their radiations overlap, a statistical phenomenon we call *Rayleigh's curse*.

Since photon shot noise is now the dominant noise source in fluorescence microscopy [8, 10] as well as stellar imaging [11–13], it is timely to inquire whether a quantum treatment can lead to new insights. Here we attack the problem from the perspective of quantum metrology, a branch of quantum information theory relevant to sensing and imaging [14, 15]. To be specific, we derive the fundamental quantum limit to the precision of locating two weak thermal optical point sources in the form of the quantum Cramér-Rao bound (QCRB) proposed by Helstrom [14]. Surprisingly, we find that the QCRB maintains a fairly constant value for any separation and shows no sign of Rayleigh's curse. This behavior is in stark contrast to the QCRB for two in-phase coherent sources, in which case Rayleigh's curse is fundamental [16].

It is known mathematically that there exists a measurement scheme to attain the QCRB for one parameter asymptotically [17, 18]. For a more concrete experimental implementation, here we propose the method of spatial-mode demultiplexing (SPADE). We show that SPADE can ideally estimate the separation between the two sources with a classical Fisher information equal to the quantum value, and we also propose linear optical system designs that can implement the measurement. Direct imaging is poor for two close sources precisely because it estimates their separation poorly [7, 8], and SPADE is able to overcome this problem and Rayleigh's curse via further linear optical processing before photon counting.

The subject of quantum imaging has been extensively studied; see, for example, Refs. [14, 16, 19–25] and Supplementary Information for an extended literature review. However, most prior proposals rely on nonclassical sources or multiphoton coincidence measurements, making them difficult and inefficient to use in practice. Incoherent sources, such as fluorophores and stars, are of course much more common, and linear optical methods to enhance the localization precision for close incoherent sources will be of monumental interest to both localization microscopy [3, 5, 6] and astrometry [11]. The most relevant prior work remains the pioneering studies by Helstrom on thermal sources [14], yet he studied two sources only in the context of binary hypothesis testing and assumed a given separation in the two-source hypothesis [19]. As the separation is usually unknown and needs to be estimated in the first place [3, 5–8], our parameter-estimation framework should be more useful.

I. QUANTUM OPTICS FOR WEAK THERMAL SOURCES

To illustrate the essential physics, we follow Lord Rayleigh's lead [1] and assume quasi-monochromatic scalar paraxial waves and one spatial dimension on the object and image planes. Within each short coherence time interval for a thermal source at optical frequencies, it is standard [12, 26, 27] to assume that the average photon number ϵ arriving on the image plane is much smaller than 1, and useful information is obtained only after many photons have been mea-

* mankei@nus.edu.sg

sured over many such intervals. For example, a star with sun-like temperature 6000 K emits $\sim 10^{-2}$ photon on average per mode at center wavelength 500 nm, and the limited fraction of the coherence area captured by the telescope aperture further reduces the received photon number [26]. In microscopy, a typical fluorophore emits $< 10^7$ photons per second [28] with coherence time < 50 fs [10], leading to $\epsilon < 10^{-6}$ for two sources. This means that the quantum density operator for the optical fields on the image plane in each coherence time interval can be well approximated as $\rho = (1 - \epsilon)\rho_0 + \epsilon\rho_1 + O(\epsilon^2)$, where $\rho_0 = |\text{vac}\rangle\langle\text{vac}|$ is the zero-photon state, ρ_1 is a one-photon state, and $O(\epsilon^2)$ denotes terms on the order of ϵ^2 (see Supplementary Information). A similar approximation was also used to study stellar interferometry in Ref. [29]. The negligence of the $O(\epsilon^2)$ multiphoton probability leads to a Poisson photon-counting distribution [26], which ignores bunching or antibunching effects but remains an excellent empirical model for both stellar optical sources [12, 13, 26, 30] and fluorophores [8, 10, 28, 31] by virtue of the $\epsilon \ll 1$ condition. For the rest of the paper, we neglect the $O(\epsilon^2)$ terms and use the \approx sign to denote approximations accurate to the first order of ϵ .

A connection with classical statistical optics can be made by observing that ρ_1 is related to the mutual coherence of the optical fields with respect to the Sudarshan-Glauber distribution [29]. For two incoherent point sources and a diffraction-limited imaging system, the one-photon state can be taken as $\rho_1 \approx (|\psi_1\rangle\langle\psi_1| + |\psi_2\rangle\langle\psi_2|)/2$, $|\psi_s\rangle = \int_{-\infty}^{\infty} dx \psi_s(x) |x\rangle$, $s = 1, 2$ (see Supplementary Information), where x is the image-plane coordinate normalized with respect to the magnification factor of the imaging system [32], $|x\rangle = a^\dagger(x)|x\rangle$ is the photon image-plane position eigenket defined with respect to annihilation and creation operators that obey $[a(x), a^\dagger(x')] = \delta(x - x')$ [20], and $\psi_s(x)$ is the image-plane wavefunction from each source.

We can reproduce the standard Poisson model of direct image-plane photon counting [8, 10, 28, 30, 31] by considering the $1 - \epsilon$ probability of no photon count and the $\epsilon \ll 1$ probability of measuring a photon. If a photon is detected, the probability density of the photon position x is $\Lambda(x) \approx (|\langle x|\psi_1\rangle|^2 + |\langle x|\psi_2\rangle|^2)/2 = [|\psi_1(x)|^2 + |\psi_2(x)|^2]/2$. With $\epsilon \ll 1$, the photon count at each pixel with width dx can be approximated as Poisson with a mean given by $\epsilon\Lambda(x)dx$. The total photon count over M coherence time intervals then remains approximately Poisson with a mean $M\epsilon\Lambda(x)dx = N\Lambda(x)dx$, where $N \equiv M\epsilon$ is the average photon number collected over the M intervals and $\Lambda(x)$ becomes the mean intensity profile. To illustrate, Fig. 1 depicts the wavefunctions and the mean intensity for a typical imaging system.

II. CLASSICAL AND QUANTUM CRAMÉR-RAO BOUNDS

To investigate the impact of measurement noise on parameter estimation, suppose that ρ depends on a set of unknown parameters denoted by $\{\theta_\mu; \mu = 1, 2, \dots\}$, and a quantum measurement is made on the image plane over the M in-

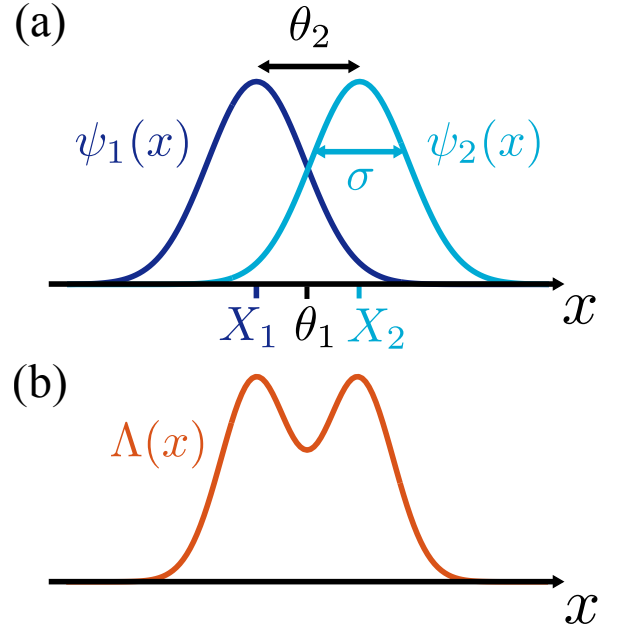


FIG. 1. (a) Two photonic wavefunctions on the image plane, each coming from a point source. X_1 and X_2 are the point-source positions, θ_1 is the centroid, θ_2 is the separation, and σ is the width of the point-spread function. (b) If photon counting is performed on the image plane, the statistics are Poisson with a mean intensity proportional to $\Lambda(x) = [|\psi_1(x)|^2 + |\psi_2(x)|^2]/2$. Note the crucial point that $\langle\psi_1|\psi_2\rangle = \int_{-\infty}^{\infty} dx \psi_1^*(x)\psi_2(x) \neq 0$, and the spatial modes excited by the two sources are in general not orthogonal, especially when Rayleigh's criterion is violated. This overlap underlies all the physical and mathematical difficulties with the resolution problem, as it implies on a fundamental level that the two modes cannot be separated for independent measurements.

tervals to estimate θ . Any quantum measurement can be mathematically described by a positive operator-valued measure (POVM) $E(\mathcal{Y})$ [14], such that the probability distribution of measurement outcome \mathcal{Y} is $P(\mathcal{Y}) = \text{tr} E(\mathcal{Y})\rho^{\otimes M}$, where tr denotes the operator trace and $\rho^{\otimes M}$ denotes a tensor product of M density operators. Let $\check{\theta}_\mu(\mathcal{Y})$ be an estimator and $\Sigma_{\mu\nu} \equiv \int d\mathcal{Y} P(\mathcal{Y})[\check{\theta}_\mu(\mathcal{Y}) - \theta_\mu][\check{\theta}_\nu(\mathcal{Y}) - \theta_\nu]$ be the error covariance matrix. For any unbiased estimator, the Cramér-Rao bound can be expressed in terms of the inequality $\Sigma_{\mu\mu} \geq (\mathcal{J}^{-1})_{\mu\mu}$ with the Fisher information matrix \mathcal{J} being a function of $P(\mathcal{Y})$ [9]. For the Poisson model of direct imaging [8, 28, 30],

$$\mathcal{J}_{\mu\nu}^{(\text{direct})} \approx N \int_{-\infty}^{\infty} dx \frac{1}{\Lambda(x)} \frac{\partial \Lambda(x)}{\partial \theta_\mu} \frac{\partial \Lambda(x)}{\partial \theta_\nu}. \quad (1)$$

As the Cramér-Rao bound is asymptotically achievable [9], the Fisher information has become the standard precision measure in modern fluorescence microscopy [31] as well as astrometry [12, 30].

Direct imaging, though standard, is but one of the infinite measurement methods permitted by quantum mechanics. The ultimate performance of any quantum measurement and any unbiased estimator can be quantified using the quantum Cramér-Rao bound $\Sigma_{\mu\mu} \geq (\mathcal{J}^{-1})_{\mu\mu} \geq (\mathcal{K}^{-1})_{\mu\mu}$, where \mathcal{K}

is the quantum Fisher information matrix in terms of ρ [14]. To compute \mathcal{K} analytically, we assume a spatially invariant imaging system with $\psi_s(x) = \psi(x - X_s)$, where $\psi(x)$ is the point-spread function of the imaging system and X_s is the unknown position of each source [32]. Both $\mathcal{J}^{(\text{direct})}$ and \mathcal{K} turn out to be diagonal if we redefine the parameters of interest as the centroid $\theta_1 = (X_1 + X_2)/2$ and the separation $\theta_2 = X_2 - X_1$, as depicted in Fig. 1. We also assume, with little loss of generality, that the point-spread function has a constant x -independent phase, which can be easily implemented by a two-lens system [32].

The computation of \mathcal{K} is described in Supplemental Information; the result is

$$\mathcal{K}_{11} \approx 4N(\Delta k^2 - \gamma^2), \quad \mathcal{K}_{22} \approx N\Delta k^2, \quad (2)$$

where $\Delta k^2 \equiv \int_{-\infty}^{\infty} dx [\psi'(x)]^2$ is the spatial-frequency variance of the real point-spread function set by the diffraction limit, while $\gamma(\theta_2) \equiv \int_{-\infty}^{\infty} dx \psi'(x)\psi(x - \theta_2)$ depends on θ_2 . The prefactor N indicates a shot-noise scaling with respect to the average photon number, as expected from classical sources [15, 16]. For $\theta_2 \rightarrow \infty$, $\gamma^2 \rightarrow 0$, and we recover the standard shot-noise limit to the localization of isolated sources.

To compare the quantum Fisher information with the classical information for direct imaging, Fig. 2(a) plots the diagonal elements of $\mathcal{J}^{(\text{direct})}$ and \mathcal{K} , assuming a Gaussian point-spread function [10] $\psi(x) = (2\pi\sigma^2)^{-1/4} \exp[-x^2/(4\sigma^2)]$, where $\sigma = \lambda/(2\pi\text{NA})$, λ is the free-space wavelength, and NA is the effective numerical aperture. With $\Delta k = 1/(2\sigma)$, the constant \mathcal{K}_{22} becomes

$$\mathcal{K}_{22} \approx \frac{N}{4\sigma^2}. \quad (3)$$

The Gaussian case is representative and the same qualitative behaviors can be observed for other common point-spread functions. For the centroid, both the classical and quantum information is within a factor of 2 of the standard limit N/σ^2 . $\mathcal{J}_{11}^{(\text{direct})} \leq \mathcal{K}_{11}$ as it should, but the small gap between the two means that there is little room for improvement.

The difference between the separation information quantities \mathcal{K}_{22} and $\mathcal{J}_{22}^{(\text{direct})}$ in Fig. 2(a) is much more dramatic. Both quantities approach the same limit $N/(4\sigma^2)$ as $\theta_2 \rightarrow \infty$, implying that direct imaging is quantum-optimal for well-separated sources. For $\theta_2/\sigma \rightarrow 0$, however, the classical information $\mathcal{J}_{22}^{(\text{direct})}$ decreases to zero. This means that direct imaging is progressively worse at estimating the separation for closer sources, to the point that the information becomes singular and the Cramér-Rao bound diverges at $\theta_2 = 0$. We call this divergent behavior due to overlapping wavefunctions Rayleigh's curse, as it implies a severe penalty on the localization precision when the intensity profiles overlap significantly and Rayleigh's criterion is violated for a given N . To expound the issue, Fig. 2(b) plots the quantum and classical Cramér-Rao bounds $1/\mathcal{K}_{22}$ and $1/\mathcal{J}_{22}^{(\text{direct})}$, demonstrating more dramatically the divergent error in the classical case and the substantial room for improvement offered by quantum mechanics.

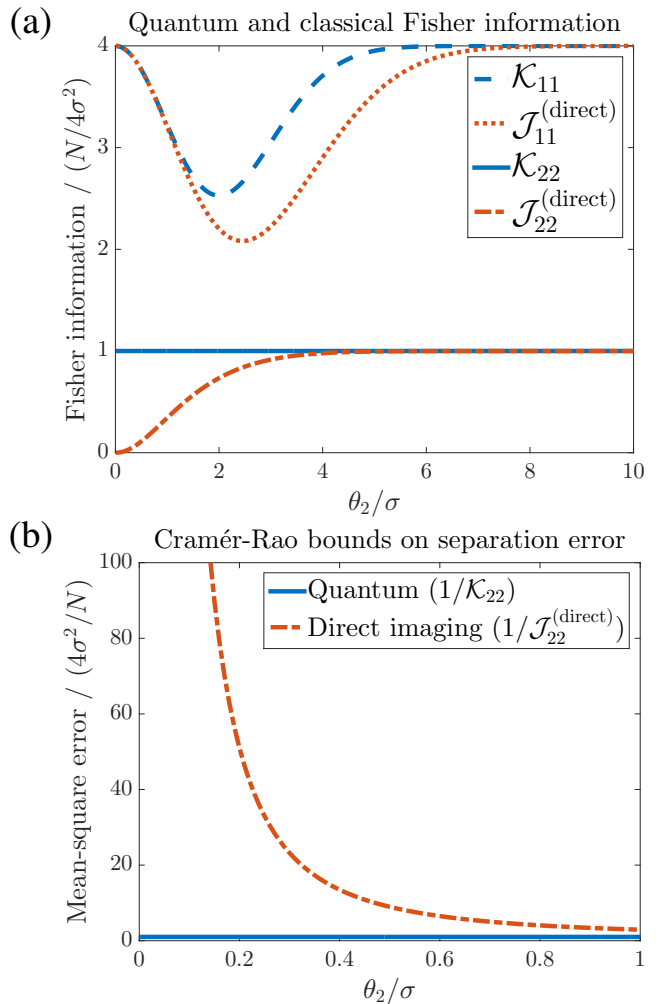


FIG. 2. (a) Plots of Fisher information versus the separation for a Gaussian point-spread function. \mathcal{K}_{11} and \mathcal{K}_{22} are the quantum values for the estimation of the centroid $\theta_1 = (X_1 + X_2)/2$ and the separation $\theta_2 = X_2 - X_1$, respectively, while $\mathcal{J}_{11}^{(\text{direct})}$ and $\mathcal{J}_{22}^{(\text{direct})}$ are the corresponding classical values for direct imaging. The horizontal axis is normalized with respect to the point-spread function width σ , while the vertical axis is normalized with respect to $N/(4\sigma^2)$, the value of \mathcal{K}_{22} . (b) The quantum Cramér-Rao bound ($1/\mathcal{K}_{22}$) and the classical bound for direct imaging ($1/\mathcal{J}_{22}^{(\text{direct})}$) on the error of separation estimation. The bounds are normalized with respect to the quantum value $4\sigma^2/N$. Rayleigh's curse refers to the divergence of the classical bound when $\theta_2 \lesssim \sigma$, as discovered by Refs. [7, 8].

Direct imaging suffers from Rayleigh's curse for any point-spread function, as $\partial\Lambda(x)/\partial\theta_2$ vanishes at $\theta_2 = 0$ while $\Lambda(x)$ remains nonzero in regions of x where the first derivative vanishes, causing $\mathcal{J}_{22}^{(\text{direct})}$ to vanish via Eq. (1). This is the reason why the Cramér-Rao bounds derived in Refs. [7, 8] for separation estimation all diverge when Rayleigh's criterion is violated. Remarkably, the quantum information \mathcal{K}_{22} in Eq. (2) stays constant regardless of the separation. If the centroid θ_1 is known, there exists a POVM with error Σ_{22} asymptotically attaining the single-parameter QCRB [17, 18], viz., $\Sigma_{22} \rightarrow 1/\mathcal{K}_{22} \approx 1/(N\Delta k^2)$, $M \rightarrow \infty$. This means

that Rayleigh's curse can be avoided for separation estimation, and considerable improvements can be obtained, if the optimal quantum measurement can be implemented.

III. SPATIAL-MODE DEMULTIPLEXING (SPADE)

Instead of measuring the position of each photon in the direct imaging method, we propose a discrimination in terms of the Hermite-Gaussian spatial modes [33] to estimate the separation between the sources. Assuming a Gaussian point-spread function and the center of the Hermite-Gaussian modes being aligned with the centroid of the two sources, it is shown in Supplementary Information that the Fisher information from the Hermite-Gaussian-basis measurement is

$$\mathcal{J}_{22}^{(\text{HG})} \approx \frac{N}{4\sigma^2}, \quad (4)$$

which is equal to the quantum information given by Eq. (3) and also independent of the true separation. This proves that the Hermite-Gaussian-basis measurement is quantum-optimal for a Gaussian point-spread function and free of Rayleigh's curse. Since centroid estimation using direct imaging is relatively insensitive to the separation, the assumption of an accurately known centroid is not difficult to satisfy (see Supplementary Information).

To measure in the Hermite-Gaussian basis, one needs to demultiplex the image-plane field in terms of the desired spatial modes before determining the outcome based on the mode in which the photon is detected. To do so with a high information-extraction efficiency, one should perform a one-to-one conversion of the Hermite-Gaussian modes into modes in a more accessible degree of freedom with minimal loss and measurements that capture as many photons as possible. For example, we can take advantage of the fact that the Hermite-Gaussian modes are waveguide modes of a quadratic-index waveguide [33]. Suppose that we couple the image-plane optical field into such a highly multimode waveguide centered at the centroid position, as shown in Fig. 3(a). Each mode with index q acquires a different propagation constant β_q along the longitudinal direction z . If a grating coupler [34] with spatial frequency κ is then used to couple all the modes into free space, each mode will be coupled to a plane wave with a different spatial frequency $\beta_q - \kappa$ along the z direction in free space, and a Fourier-transform lens can be used to focus the different plane waves onto different spots of a photon-counting array in the far field. An alternative is to use evanescent coupling with different single-mode waveguides [35], as depicted in Fig. 3(b). If each single-mode waveguide is fabricated to have a propagation constant equal to a different value of β_q , the phase-matching condition will cause each mode in the multimode waveguide to be coupled to a specific fiber.

Given these physical setups, we can now explain the operation of SPADE in a more intuitive semiclassical optics language: it is based on the exquisite sensitivity of the mode-coupling efficiencies to the offset of each wavefunction from the centroid. The incoherent sources are literally blinking on the fundamental coherence time scale, causing each image-plane photon to have a wavefunction given randomly by $\psi_1(x)$

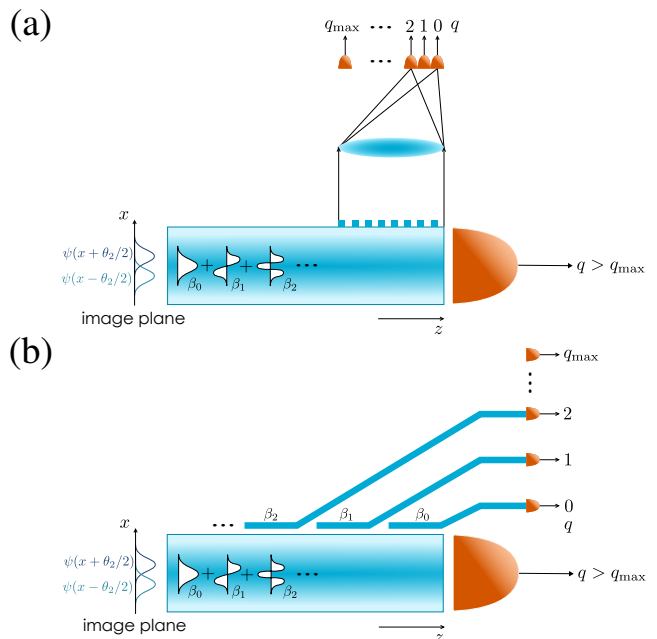


FIG. 3. (a) A multimode-waveguide SPADE with a grating output coupler and farfield photon counting. The photon counter at the end of the multimode waveguide captures any remaining photon in the higher-order or leaky modes. (b) An alternative design, with evanescent coupling to single-mode waveguides with different propagation constants for phase matching. The photon counter at the end of the multimode waveguide captures any remaining photon in the higher-order or leaky modes.

or $\psi_2(x)$. Either wavefunction can excite the waveguide modes coherently with the same excitation probabilities, such that the final photon counts become as sensitive to the offset for two sources as it is for one. Counterintuitively, it is the incoherence between the two sources that enables coupling into the first-order odd mode, which is the main spatial mode responsible for the high sensitivity to small offsets.

Since direct imaging has trouble estimating the separation only when θ_2/σ is small, and only low-order Hermite-Gaussian modes in SPADE are excited significantly in that case, we can focus on the discrimination of low-order modes to simplify the SPADE design while retaining a near-optimal precision (see Supplementary Information). The maximum-likelihood estimators for the SPADE schemes are also fortuitously simple. The photon-counting statistics are Poisson under the $\epsilon \ll 1$ condition, meaning that a time-resolved record is not necessary, and one can simply use the set of accumulated photon counts as sufficient statistics, which can be highly compressed for the simplified SPADE designs. Supplementary Information derives the estimators and also investigates the estimation errors for finite photon numbers and the issues of unknown centroid, misalignment, other point-spread functions, and two-dimensional imaging.

IV. DISCUSSION

We have presented two important results in this paper: the fundamental quantum limit to locating two incoherent optical point sources and the SPADE measurement schemes for quantum-optimal separation estimation. The quantum bound for separation estimation can be significantly lower than the classical bound for direct imaging, while SPADE can extract the full information offered by quantum mechanics via linear photonics. The proposed SPADE schemes work well for close sources with significant overlap in their wavefunctions, avoiding Rayleigh’s curse and the divergent error that plagues direct imaging. The computational simplicity of the estimators is an additional advantage.

Since the completion of this work, we have developed a semiclassical Poissonian photodetection theory [36] that can reproduce many of the results presented here, albeit with less generality, for paedagogical purposes. A generalization of our theory to two dimensions, with similar conclusions, will be presented elsewhere [37]. We have very recently derived the QCRB for thermal sources without the $\epsilon \ll 1$ approximation using an alternative method [38], validating the result

presented here, and discovered an alternative interferometric scheme that can overcome Rayleigh’s curse for thermal sources with arbitrary ϵ in two dimensions without the need to tailor the device to the point-spread function [39]. Our preliminary study also suggests that SPADE can overcome Rayleigh’s curse and saturate the quantum bound for thermal sources with arbitrary ϵ [40].

V. ACKNOWLEDGMENTS

We acknowledge useful discussions with Shan Zheng Ang and Shilin Ng. **Funding:** This work is supported by the Singapore National Research Foundation under NRF Grant No. NRF-NRFF2011-07 and the Singapore Ministry of Education Academic Research Fund Tier 1 Project R-263-000-C06-112. **Author contributions:** M. T. developed the basic quantum optics formalism and conceived the idea of applying quantum metrology to two-incoherent-source localization. R. N. derived the quantum Fisher information with X.-M. L. and M. T.’s inputs and checks. M. T. invented and analyzed the SPADE measurement schemes and wrote the paper. All authors discussed extensively during the course of this work.

SUPPLEMENTARY INFORMATION

Appendix A: Quantum-imaging literature review

Helstrom pioneered the application of his quantum estimation and detection bounds to optical imaging problems [14, 19, 41], focusing on coherent and thermal sources. In particular, the now well-known expression for the shot-noise-limited localization error for one source can be found in Ref. [41]; similar expressions in the context of direct imaging were later reported in Refs. [30, 42, 43]. For more recent studies of quantum metrology for coherent-state or nonclassical-state imaging, see, for example, Refs. [44–46]. For studies on the use of squeezed light for single-object localization, see, for example, Refs. [16, 47–50]. All of these works did not consider the problem of locating two close incoherent sources.

The standard quantum model of paraxial imaging and the use of nonclassical light for that purpose were proposed by Yuen and Shapiro [20]. This topic has been further investigated most notably by Kolobov and co-workers [21, 51], with focus on coherent or squeezed light, homodyne detection, and field fluctuations. Such models are irrelevant to incoherent sources such as stars and fluorophores, for which the mean field is zero and photon counting is the more relevant method to minimize vacuum noise. Subsequent work by Kolobov and co-workers [52–55] considers the squeezing and measurement of the eigenmodes of an imaging system for image-reconstruction superresolution. Again, these studies focus on coherent or squeezed light.

The “Rayleigh resolution limit” mentioned by many of these papers is a misnomer, as the resolution limit for coherent imaging should be attributed to Abbe, while Rayleigh’s criterion is defined in terms of two incoherent sources [1]. As mentioned in Ref. [54], “*The second generalization of the quantum theory of superresolution presented in this paper is from coherent imaging into partially coherent and fully incoherent cases. This problem is very challenging and will be addressed in forthcoming publications.*” Unfortunately, these authors have not yet addressed this challenging problem in their publications since then. The eigenmodes they studied are in any case unrelated to the spatial modes we propose for the two-source localization problem.

We can consider the schemes proposed in Refs. [56–63] as another class of superresolution imaging protocols, which do not consider statistical inference and require coherent or nonclassical sources and multiphoton coincidence measurements. It is well known in statistical optics that multiphoton coincidence measurements, such as Hanbury-Brown Twiss interferometry, has a much poorer signal-to-noise ratio than amplitude interferometry because multiphoton coincidence events are rare for thermal optical sources [26, 29]. The actual statistical resolution of this class of protocols is thus questionable, especially for weak sources, without further proofs in the context of inference accuracy. In recent years, there has also been significant interest in quantum lithography [23, 25, 64, 65] and ghost imaging [23, 24, 66, 67], although their applications are clearly different from our purpose and will not be elaborated here.

The relative neglect of incoherent sources in the quantum imaging literature, despite their obvious importance, may be due to a lack of appreciation that quantum mechanics can be relevant to such highly classical light. Our work thus showcases quantum

metrology as a powerful tool to discover the ultimate performance of sensing and imaging even in the apparently classical regime, providing not only rigorous quantum limits but also pleasant surprises for one of the most important applications in optics.

Appendix B: Quantum optics for weak thermal sources

Define $\alpha = (\alpha_1, \dots, \alpha_J)^\top$ as a column vector of complex field amplitudes for J optical modes on the image plane and $|\alpha\rangle$ as a multimode coherent state with amplitude α . Any quantum state can be expressed as

$$\rho = \int D\alpha \Phi(\alpha) |\alpha\rangle \langle \alpha|, \quad (\text{B1})$$

where $\Phi(\alpha)$ is the Sudarshan-Glauber representation and $D\alpha$ is an appropriate measure [27]. For thermal sources, it is standard [27] to assume Φ to be a zero-mean complex Gaussian given by

$$\Phi(\alpha) = \frac{1}{\det(\pi\Gamma)} \exp(-\alpha^\dagger \Gamma^{-1} \alpha), \quad (\text{B2})$$

where $\alpha^\dagger = (\alpha_1^*, \dots, \alpha_J^*)$ denotes the complex transpose of α ,

$$\Gamma = \mathbb{E}(\alpha \alpha^\dagger) \quad (\text{B3})$$

is the image-plane mutual coherence matrix, and $\mathbb{E}[f(\alpha)] \equiv \int D\alpha \Phi(\alpha) f(\alpha)$ denotes the expectation of any function f with respect to the Φ distribution. Writing the coherent state in terms of a superposition of Fock states and applying the Gaussian moment theorem [27] to Eq. (B1), we can express ρ as the incoherent mixture

$$\rho = \sum_{n=0}^{\infty} \pi_n \rho_n, \quad n \equiv \sum_j n_j, \quad (\text{B4})$$

where π_n is the probability of having n total photons in the state and ρ_n is a multimode n -photon Fock state.

At optical frequencies or beyond, it is standard [12, 13, 26, 27, 29] to assume that, within the short coherence time of a source, the average photon number arriving at the imaging device is much smaller than 1. We will make the same assumption for two sources, viz.,

$$\epsilon \equiv \sum_j \text{tr} \rho a_j^\dagger a_j = \mathbb{E}(\alpha^\dagger \alpha) = \sum_j \Gamma_{jj} \ll 1, \quad (\text{B5})$$

where tr denotes the operator trace, a_j is the annihilation operator for the j th mode, and a_j^\dagger is the creation operator. The zero-photon probability given by

$$\pi_0 = \mathbb{E}(e^{-\alpha^\dagger \alpha}) = 1 - \epsilon + O(\epsilon^2) \quad (\text{B6})$$

is then the highest, with $O(\epsilon^2)$ denoting terms on the order of ϵ^2 . The one-photon probability given by

$$\pi_1 = \mathbb{E}(e^{-\alpha^\dagger \alpha} \alpha^\dagger \alpha) = \epsilon + O(\epsilon^2) \quad (\text{B7})$$

is ϵ to the first order, and the multiphoton probability

$$\sum_{n=2}^{\infty} \pi_n = 1 - \pi_0 - \pi_1 = O(\epsilon^2) \quad (\text{B8})$$

is in the second order, leading to

$$\rho = (1 - \epsilon)\rho_0 + \epsilon\rho_1 + O(\epsilon^2). \quad (\text{B9})$$

As the vacuum state provides no information and multiphoton events are rare, we will focus on the one-photon state ρ_1 . This focus also makes our formalism applicable to inefficient single-photon emitters that may have non-Poissonian multiphoton

statistics but the multiphoton events are too rare to be relevant. In the following we use the \approx sign to denote approximations accurate to the first order of ϵ .

Define $|j\rangle = a_j^\dagger |\text{vac}\rangle$ as the ket with one photon only in the j th mode. Consider the one-photon matrix elements

$$\langle j | \rho | k \rangle = \mathbb{E} \left(e^{-\alpha^\dagger \alpha} \alpha_j \alpha_k^* \right) = \Gamma_{jk} + O(\epsilon^2). \quad (\text{B10})$$

We can then assume, to the first order of ϵ ,

$$\pi_1 \approx \epsilon, \quad \rho_1 \approx \frac{1}{\epsilon} \sum_{j,k} \Gamma_{jk} |j\rangle \langle k|. \quad (\text{B11})$$

Similar approximations are also used in Refs. [29, 68]. To derive Γ , let $\beta \equiv (\beta_1, \dots, \beta_K)^\top$ be the field amplitudes for optical modes on the object plane, and consider the field propagation rule $\alpha = S\beta$ for a linear optical system, where S is the field scattering matrix. The image-plane mutual coherence Γ is then related to the object-plane mutual coherence matrix $\Gamma^{(\circ)}$ by

$$\Gamma = S\Gamma^{(\circ)}S^\dagger. \quad (\text{B12})$$

This propagation rule is a basic principle in both classical and quantum statistical optics [27].

In the paraxial regime, we can use localized wavepacket modes as a basis [20]. Let u be the position index for a wavepacket mode on the one-dimensional object plane and consider two incoherent sources with equal intensities at positions $u = u_1$ and $u = u_2$. The fields are uncorrelated at different points on the object plane, with nonzero intensities only at the sources. Then

$$\Gamma_{uv}^{(\circ)} = \epsilon_0 \delta_{uv} (\delta_{uu_1} + \delta_{uu_2}), \quad (\text{B13})$$

where ϵ_0 is the average photon number from each source. On the image plane, the mutual coherence becomes

$$\Gamma_{jk} = \epsilon_0 [S(j, u_1)S^*(k, u_1) + S(j, u_2)S^*(k, u_2)], \quad (\text{B14})$$

and the average photon number can be expressed as $\epsilon = 2\epsilon_0\eta$, where $\eta \equiv \sum_j |S(j, u_s)|^2$ is the quantum efficiency of the imaging system and we have made the reasonable assumption that the efficiency is the same for both sources. Equation (B11) can then be expressed as

$$\rho_1 \approx \frac{1}{2} (|\psi_1\rangle \langle \psi_1| + |\psi_2\rangle \langle \psi_2|), \quad (\text{B15})$$

if we define single-photon kets $|\psi_s\rangle \equiv \sum_j \psi(j, u_s) |j\rangle$ with normalized wavefunctions $\psi(j, u_s) = S(j, u_s)/\sqrt{\eta}$. Assuming image-plane wavepacket positions $x_j = x_0 + jd_x$, position eigenkets $|x_j\rangle = |j\rangle/\sqrt{d_x}$, and wavefunctions $\psi_s(x_j) = \psi(j, u_s)/\sqrt{d_x}$, we arrive at

$$|\psi_s\rangle = \int_{-\infty}^{\infty} dx \psi_s(x) |x\rangle, \quad s = 1, 2, \quad (\text{B16})$$

by taking the continuous-space limit with infinitesimal dx [20].

Appendix C: Quantum metrology

The quantum Fisher information matrix with respect to ρ proposed by Helstrom [14] is defined as

$$\mathcal{K}_{\mu\nu}(\rho) = M \text{Re tr } \mathcal{L}_\mu(\rho)\mathcal{L}_\nu(\rho)\rho, \quad (\text{C1})$$

where $\mathcal{L}_\mu(\rho)$ is a symmetric logarithmic derivative (SLD) of ρ . Writing ρ in its eigenbasis as

$$\rho = \sum_j D_j |e_j\rangle \langle e_j|, \quad (\text{C2})$$

$\mathcal{L}_\mu(\rho)$ can be expressed as [14]

$$\mathcal{L}_\mu(\rho) = \sum_{j,k; D_j + D_k \neq 0} \frac{2}{D_j + D_k} \langle e_j | \frac{\partial \rho}{\partial \theta_\mu} | e_k \rangle |e_j\rangle \langle e_k|. \quad (\text{C3})$$

Given this definition and Eq. (B4), it can be shown that

$$\mathcal{K}(\rho) = \sum_n \pi_n \mathcal{K}(\rho_n) \geq \pi_1 \mathcal{K}(\rho_1), \quad (\text{C4})$$

as each ρ_n is in an orthogonal subspace. Since the vacuum state $\rho_0 = |\text{vac}\rangle \langle \text{vac}|$ contains no information and multiphoton events are rare, the total information will be dominated by that from the one-photon state ρ_1 . We will therefore focus on the one-photon component $\pi_1 \mathcal{K}(\rho_1)$ as a tight lower bound on the quantum information and assume in the following

$$\mathcal{K}(\rho) \approx \pi_1 \mathcal{K}(\rho_1). \quad (\text{C5})$$

With $\pi_1 \approx \epsilon$ and the probability of multiphoton events being $O(\epsilon^2)$ according to Eq. (B8), this approximation is accurate to the first order of ϵ .

To compute the quantum Fisher information matrix $\mathcal{K}(\rho_1)$ according to Eqs. (C1)–(C3), we first need to diagonalize the ρ_1 in Eqs. (B15) and (B16), noting that the eigenvectors should span the support of $\partial\rho_1/\partial\theta_\mu$. The partial derivative of ρ_1 with respect to X_μ can be expressed as

$$\frac{\partial\rho_1}{\partial X_\mu} = \frac{\partial D_1}{\partial X_\mu} |e_1\rangle \langle e_1| + \frac{\partial D_2}{\partial X_\mu} |e_2\rangle \langle e_2| + \left[D_1 \frac{\partial |e_1\rangle}{\partial X_\mu} \langle e_1| + D_2 \frac{\partial |e_2\rangle}{\partial X_\mu} \langle e_2| + \text{H.c.} \right], \quad (\text{C6})$$

where H.c. denotes the Hermitian conjugate. In addition to the support of ρ_1 spanned by $|e_1\rangle$ and $|e_2\rangle$, we also need to find more eigenvectors that span the support of $\partial |e_1\rangle / \partial X_\mu$ and $\partial |e_2\rangle / \partial X_\mu$.

Assuming that $\psi_\mu(x) = \psi(x - X_\mu)$ and the point-spread function $\psi(x)$ has an x -independent phase, we can take $\psi(x)$ to be real without loss of generality and choose the following orthonormal set of eigenvectors:

$$\begin{aligned} |e_1\rangle &= \frac{1}{\sqrt{2(1-\delta)}} (|\psi_1\rangle - |\psi_2\rangle), & |e_3\rangle &= \frac{1}{c_3} \left[\frac{\Delta k}{\sqrt{2}} (|\psi_{11}\rangle + |\psi_{22}\rangle) - \frac{\gamma}{\sqrt{1-\delta}} |e_1\rangle \right], \\ |e_2\rangle &= \frac{1}{\sqrt{2(1+\delta)}} (|\psi_1\rangle + |\psi_2\rangle), & |e_4\rangle &= \frac{1}{c_4} \left[\frac{\Delta k}{\sqrt{2}} (|\psi_{11}\rangle - |\psi_{22}\rangle) + \frac{\gamma}{\sqrt{1+\delta}} |e_2\rangle \right], \end{aligned} \quad (\text{C7})$$

where

$$\begin{aligned} \Delta k^2 &\equiv \int_{-\infty}^{\infty} dx \left[\frac{\partial\psi(x)}{\partial x} \right]^2, & c_3 &\equiv \left(\Delta k^2 + b^2 - \frac{\gamma^2}{1-\delta} \right)^{1/2}, \\ \gamma(\theta_2) &\equiv \int_{-\infty}^{\infty} dx \frac{\partial\psi(x)}{\partial x} \psi(x - \theta_2), & c_4 &\equiv \left(\Delta k^2 - b^2 - \frac{\gamma^2}{1+\delta} \right)^{1/2}, \\ |\psi_{11}\rangle &\equiv \frac{1}{\Delta k} \int_{-\infty}^{\infty} dx \frac{\partial\psi(x - X_1)}{\partial X_1} |x\rangle, & b^2 &\equiv \int_{-\infty}^{\infty} dx \frac{\partial\psi(x - X_1)}{\partial X_1} \frac{\partial\psi(x - X_2)}{\partial X_2}, \\ |\psi_{22}\rangle &\equiv \frac{1}{\Delta k} \int_{-\infty}^{\infty} dx \frac{\partial\psi(x - X_2)}{\partial X_2} |x\rangle, & \delta &\equiv \int_{-\infty}^{\infty} dx \psi(x - X_1) \psi(x - X_2), \end{aligned} \quad (\text{C8})$$

and the eigenvalues of ρ_1 are

$$D_1 = \frac{1-\delta}{2}, \quad D_2 = \frac{1+\delta}{2}, \quad D_3 = D_4 = 0. \quad (\text{C9})$$

After more algebra, the SLD in Eq. (C3) with respect to the derivative in Eq. (C6) can be expressed as

$$\mathcal{L}_\mu^{(X)} = \sum_{j,k} \mathcal{L}_{\mu,jk}^{(X)} |e_j\rangle \langle e_k| \quad (\text{C10})$$

with a real and symmetric matrix $\mathcal{L}_{\mu,jk}^{(X)} = \mathcal{L}_{\mu,kj}^{(X)}$, the nonzero and unique elements of which are found to be

$$\begin{aligned} \mathcal{L}_{1,11}^{(X)} &= -\mathcal{L}_{2,11}^{(X)} = \frac{\gamma}{1-\delta}, \\ \mathcal{L}_{1,12}^{(X)} &= \mathcal{L}_{2,12}^{(X)} = \frac{\gamma\delta}{\sqrt{1-\delta^2}}, & \mathcal{L}_{1,13}^{(X)} &= -\mathcal{L}_{2,13}^{(X)} = \frac{c_3}{\sqrt{1-\delta}}, & \mathcal{L}_{1,14}^{(X)} &= \mathcal{L}_{2,14}^{(X)} = \frac{c_4}{\sqrt{1-\delta}}, \\ \mathcal{L}_{1,22}^{(X)} &= -\mathcal{L}_{2,22}^{(X)} = \frac{-\gamma}{1+\delta}, & \mathcal{L}_{1,23}^{(X)} &= \mathcal{L}_{2,23}^{(X)} = \frac{c_3}{\sqrt{1+\delta}}, & \mathcal{L}_{1,24}^{(X)} &= -\mathcal{L}_{2,24}^{(X)} = \frac{c_4}{\sqrt{1+\delta}}. \end{aligned} \quad (\text{C11})$$

In terms of the centroid and separation parameters given by $\theta_1 = (X_1 + X_2)/2$ and $\theta_2 = X_2 - X_1$, the SLDs become

$$\mathcal{L}_1 = \mathcal{L}_1^{(X)} + \mathcal{L}_2^{(X)}, \quad \mathcal{L}_2 = \frac{\mathcal{L}_2^{(X)} - \mathcal{L}_1^{(X)}}{2}. \quad (\text{C12})$$

We can now substitute Eqs. (C9)–(C12) into Eq. (C1) to compute the quantum Fisher information matrix $\mathcal{K}(\rho_1)$. The final result, assuming $M\pi_1 \approx M\epsilon = N$, is given by

$$\mathcal{K}_{11} \approx 4N(\Delta k^2 - \gamma^2), \quad \mathcal{K}_{22} \approx N\Delta k^2, \quad (\text{C13})$$

with $\mathcal{K}_{12} = \mathcal{K}_{21} = 0$, as stated in the main text.

Appendix D: Spatial-mode demultiplexing (SPADE)

Consider the discrete Hermite-Gaussian basis $\{|\phi_q\rangle; q = 0, 1, \dots\}$, where

$$|\phi_q\rangle = \int_{-\infty}^{\infty} dx \phi_q(x) |x\rangle, \quad q = 0, 1, \dots \quad (\text{D1})$$

$$\phi_q(x) = \left(\frac{1}{2\pi\sigma^2}\right)^{1/4} \frac{1}{\sqrt{2^q q!}} H_q\left(\frac{x}{\sqrt{2}\sigma}\right) \exp\left(-\frac{x^2}{4\sigma^2}\right), \quad (\text{D2})$$

and H_q is the Hermite polynomial [33]. The POVM for each coherence time interval can be expressed as projections

$$E_0 = |\text{vac}\rangle\langle\text{vac}|, \quad E_1(q) = |\phi_q\rangle\langle\phi_q|. \quad (\text{D3})$$

Conditioned on a detection event, the probability of detecting the photon in the q th mode becomes

$$P_1(q) \approx \frac{1}{2} \left(|\langle\phi_q|\psi_1\rangle|^2 + |\langle\phi_q|\psi_2\rangle|^2 \right). \quad (\text{D4})$$

Similar to direct imaging, $\epsilon \ll 1$ implies that, over M intervals, the total photon count m_q in each Hermite-Gaussian mode can be approximated as Poisson with a mean given by $NP_1(q)$.

To proceed further, we assume that the centroid θ_1 is known, and only θ_2 is to be estimated. Let $\theta_1 = 0$ without loss of generality, and the wavefunctions become $\psi_1(x) = \psi(x + \theta_2/2)$, and $\psi_2(x) = \psi(x - \theta_2/2)$. For simple analytic results, we further assume that the point-spread function is Gaussian. The overlap factors in Eq. (D4) can be evaluated by recognizing that $|\phi_q\rangle$ is mathematically equivalent to an energy eigenstate of a harmonic oscillator (in the configuration space of the photon), and $|\psi_1\rangle$ and $|\psi_2\rangle$ are equivalent to configuration-space coherent states with displacements $\pm\theta_2/(4\sigma)$. The result is

$$P_1(q) \approx |\langle\phi_q|\psi_1\rangle|^2 = |\langle\phi_q|\psi_2\rangle|^2 = \exp(-Q) \frac{Q^q}{q!}, \quad Q \equiv \frac{\theta_2^2}{16\sigma^2}. \quad (\text{D5})$$

This formula is valid even if the two sources have unequal intensities and ρ_1 is any mixture of $|\psi_1\rangle\langle\psi_1|$ and $|\psi_2\rangle\langle\psi_2|$. The classical Fisher information for the Hermite-Gaussian-basis measurement over M intervals becomes

$$\mathcal{J}_{22}^{(\text{HG})} \approx N \sum_{q=0}^{\infty} P_1(q) \left[\frac{\partial}{\partial\theta_2} \ln P_1(q) \right]^2 = \frac{N}{4\sigma^2}, \quad (\text{D6})$$

which is the result in the main text.

Suppose that a total of L photons are detected over the M trials. A record of the modes for the L photons (q_1, \dots, q_L) can be obtained, but in fact a time-resolved record is not necessary, as $\sum_l q_l$ is a sufficient statistic for estimating Q and θ_2 [69], meaning that the set of photon numbers $\{m_q = \sum_l \delta_{qq_l}; q = 0, 1, \dots\}$ detected in different modes are also sufficient. The maximum-likelihood estimator becomes

$$\check{Q}_{\text{ML}} = \frac{1}{L} \sum_q q m_q, \quad \check{\theta}_{2\text{ML}} = 4\sigma \sqrt{\check{Q}_{\text{ML}}}. \quad (\text{D7})$$

For $L = 0$, one can set $\check{\theta}_2$ to a constant value; the $L = 0$ probability $(1 - \epsilon)^M \approx \exp(-N)$ is in any case negligible for large N . Maximum-likelihood estimation can asymptotically saturate the Cramér-Rao bound $\Sigma_{22} \geq 1/\mathcal{J}_{22}^{(\text{HG})}$ for large M [69]. With $\mathcal{J}_{22}^{(\text{HG})} \approx \mathcal{K}_{22}$, the QCRB is asymptotically attainable as well.

Appendix E: Binary SPADE

Since direct imaging has trouble estimating the separation only when θ_2/σ is small, and only low-order Hermite-Gaussian modes in SPADE are excited significantly in that case, we can focus on the discrimination of low-order modes to simplify the SPADE design. One such design is depicted in Fig. 4(a), where only the $q = 0$ component is coupled into the single-mode waveguide, while any photon in the higher-order modes remains in the multimode waveguide for subsequent detection. An alternative design is depicted in Fig. 4(b): the $q = 0$ mode is coupled to a single-mode waveguide, while higher-order modes are necessarily coupled to the leaky modes of the waveguide, which are also measured.

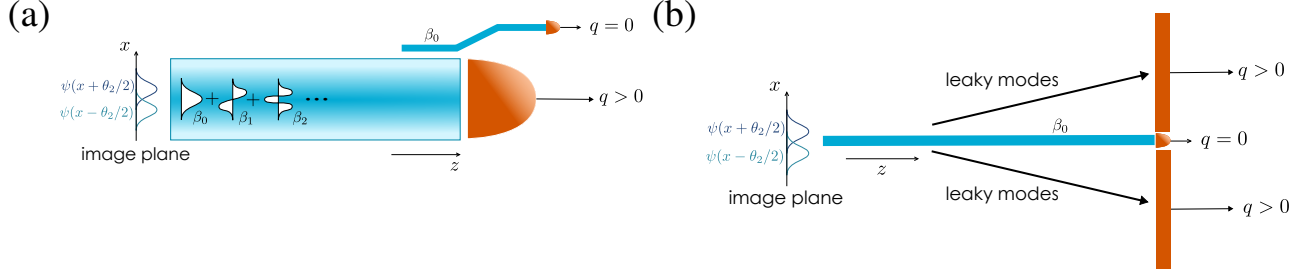


FIG. 4. (a) Binary SPADE with evanescent coupling to only one single-mode waveguide. (b) An alternative design with a single-mode waveguide and leaky-mode detection.

Conditioned on a detection event, the probability of detecting the photon in the $q = 0$ mode remains

$$P_1(q = 0) \approx \exp(-Q), \quad (\text{E1})$$

but now the higher-order modes cannot be discriminated, and the probability of detecting a photon in any higher-order mode becomes

$$P_1(q > 0) = 1 - P_1(q = 0) \approx 1 - \exp(-Q). \quad (\text{E2})$$

The Fisher information for this scheme is hence

$$\mathcal{J}_{22}^{(b)} \approx \frac{N}{4\sigma^2} \frac{Q \exp(-Q)}{1 - \exp(-Q)}. \quad (\text{E3})$$

Figure 5 compares $\mathcal{J}_{22}^{(b)}$ with $\mathcal{J}_{22}^{(\text{HG})} \approx \mathcal{K}_{22}$ as well as $\mathcal{J}_{22}^{(\text{direct})}$ for direct imaging. It can be seen that binary SPADE gives significant information for small θ_2/σ , precisely in the region where direct imaging performs poorly. Binary SPADE actually works less well when the sources are far apart, and the two methods can complement each other to enhance the localization precision, as shown in Sec. F.

For a total of L detected photons, m_0 , the number of photons detected in the $q = 0$ mode, is a sufficient statistic for estimating Q and θ_2 and follows the binomial distribution with success probability $\exp(-Q)$ [69]. The maximum-likelihood estimator becomes

$$\check{Q}_{\text{ML}}^{(b)} = -\ln \frac{m_0}{L}, \quad \check{\theta}_{2\text{ML}}^{(b)} = 4\sigma \sqrt{\check{Q}_{\text{ML}}^{(b)}}. \quad (\text{E4})$$

For $L = 0$ or $m_0 = 0$, one can select finite values for $\check{\theta}_2$ to regularize the estimator.

Compared with the large amount of data generated by direct imaging and the complex algorithms needed to process them, only two photon numbers are needed by binary SPADE to estimate the separation precisely. The highly compressed measurement output, enabled by the optical processing, is a bonus in practice.

Appendix F: Unknown centroid and misalignment

Our analysis of SPADE thus far assumes that the centroid of the two sources is known exactly and the device is optimally aligned with the centroid. For astronomy, it is reasonable to assume that the centroid is known accurately, as extensive telescopic data on stellar objects should be readily available and conventional imaging is accurate in estimating the centroid. Even if the centroid is unknown, stellar objects usually shine long enough for one to collect ample prior information before aligning the SPADE device. For microscopy, however, biological samples can move more quickly and fluorophores can bleach, giving little

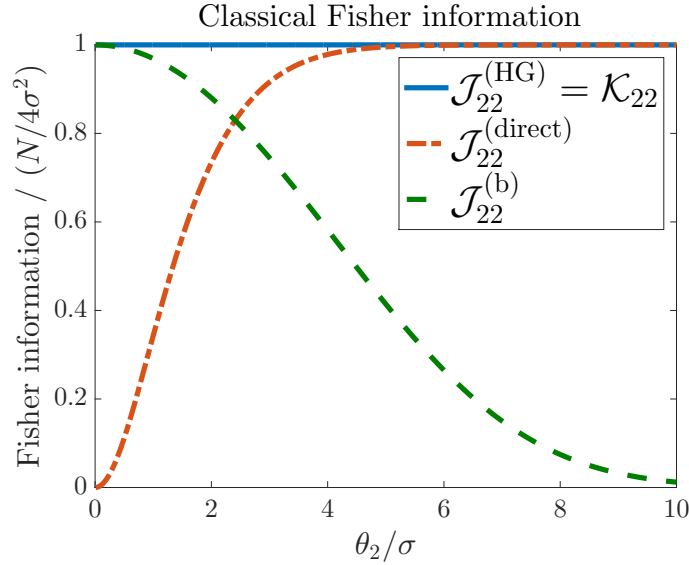


FIG. 5. Fisher information for separation estimation versus normalized separation θ_2/σ for a Gaussian point-spread function. $\mathcal{J}_{22}^{(\text{HG})}$ is the information for the ideal Hermite-Gaussian-basis measurement, which is equal to the quantum value \mathcal{K}_{22} , $\mathcal{J}_{22}^{(\text{direct})}$ is for direct imaging, and $\mathcal{J}_{22}^{(\text{b})}$ is for binary SPADE. The vertical axis is normalized with respect to $\mathcal{J}_{22}^{(\text{HG})} = \mathcal{K}_{22} = N/(4\sigma^2)$.

time and few photons for one to estimate both parameters. One option, to be explored in future work, is to scan the SPADE device across the image plane in a manner similar to the operation of a confocal microscope [10].

Another option, illustrated in Fig. 6, is to split the optical field by a beam splitter, measure one output port by conventional photon-counting imaging, and use the centroid estimate to align SPADE at the other port in a hybrid scheme. As the overall optical system is linear with photon counting, the output statistics remain Poisson for $\epsilon \ll 1$, meaning that the statistics of the measurements are independent and can be analyzed separately. The penalty of beam-splitting with the classical sources is simply a reduction of photon number at each port. With direct imaging offering little information about θ_2 when Rayleigh's criterion is violated, the additional information offered by SPADE for a reduced photon number can still be helpful. The outstanding issues are then the robustness of SPADE to the misalignment due to imperfect centroid estimation, and the overhead resources of photons needed to achieve satisfactory alignment.

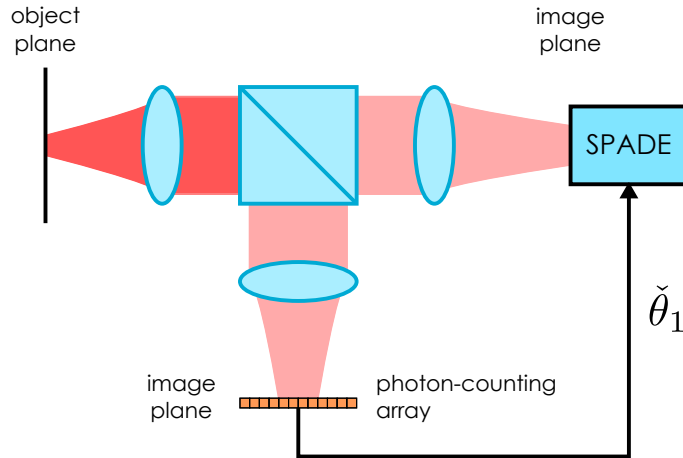


FIG. 6. A hybrid measurement scheme that splits the optical field by a beam splitter, measures one output port by a photon-counting array, and use the centroid estimate $\check{\theta}_1$ to align SPADE at the other port.

Let the center of a SPADE device be $\check{\theta}_1$ and consider $\theta_1 \neq \check{\theta}_1$ due to misalignment. For a Gaussian point-spread function and

the Hermite-Gaussian-basis measurement, Eq. (D4) should be generalized to

$$P_1(q) \approx \frac{1}{2} \left[\exp(-Q_1) \frac{Q_1^q}{q!} + \exp(-Q_2) \frac{Q_2^q}{q!} \right],$$

$$Q_1 \equiv \frac{1}{4\sigma^2} \left(\check{\theta}_1 - \theta_1 + \frac{\theta_2}{2} \right)^2, \quad Q_2 \equiv \frac{1}{4\sigma^2} \left(\check{\theta}_1 - \theta_1 - \frac{\theta_2}{2} \right)^2. \quad (\text{F1})$$

Define the level of misalignment as

$$\xi \equiv \frac{|\check{\theta}_1 - \theta_1|}{\sigma}. \quad (\text{F2})$$

We treat ξ as a systematic error and θ_2 as the parameter of interest for SPADE. Figure 7(a) plots the resulting Fisher information for several levels of misalignment. It can be seen that the information degrades with misalignment, but appreciable enhancements over direct imaging are still present even if $\theta_2 \ll \sigma$ and the wavefunction overlap is significant, as long as $\xi \ll 1$.

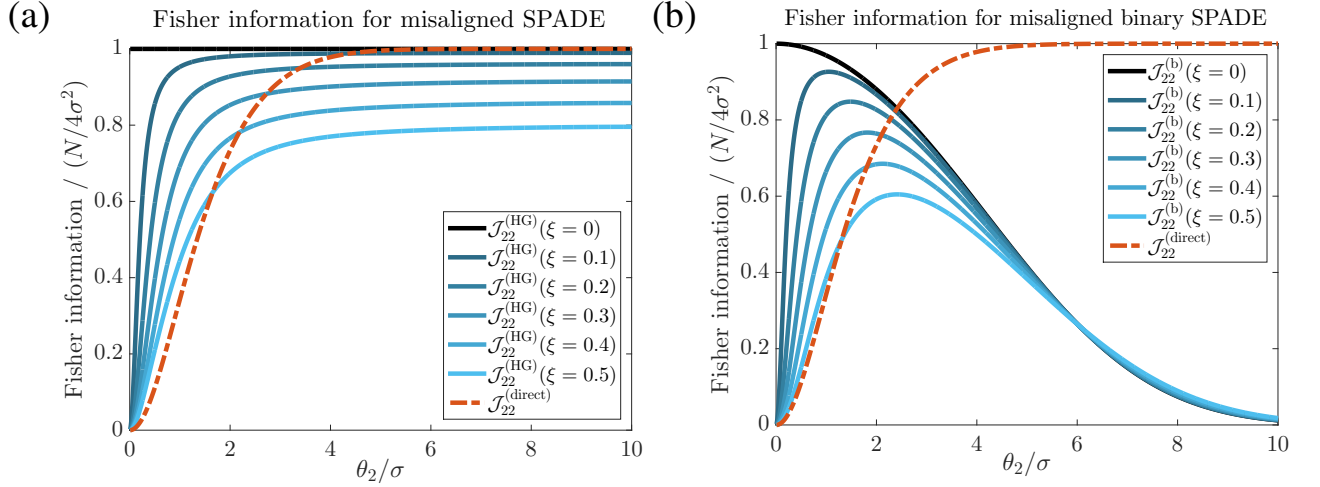


FIG. 7. Fisher information for separation estimation with (a) SPADE and (b) binary SPADE with misalignment levels $\xi = 0, 0.1, \dots, 0.5$ (solid curves) and direct imaging (dash-dotted curve). The different solid curves can be distinguished by their lower values with larger misalignments.

To attain a tolerable level of misalignment, θ_1 first needs to be estimated and $\check{\theta}_1$ should be aligned with the estimate. With conventional imaging, the centroid estimation error is near-optimal and on the order of σ/\sqrt{N} in terms of the root-mean-square value, meaning that the number of extra photons N_1 needed to attain ξ is roughly

$$N_1 \sim \frac{1}{\xi^2}. \quad (\text{F3})$$

An even more realistic analysis would take $\check{\theta}_1$ to be a stochastic waveform determined by the centroid measurements and the adaptive alignment control [70].

For binary SPADE, Eqs. (E1) and (E2) should be generalized to

$$P_1(q=0) \approx \frac{1}{2} [\exp(-Q_1) + \exp(-Q_2)], \quad P_1(q>0) \approx 1 - \frac{1}{2} \exp(-Q_1) - \frac{1}{2} \exp(-Q_2). \quad (\text{F4})$$

Figure 7(b) plots the Fisher information for misaligned binary SPADE, showing a similar degradation behavior to that in Fig. 7(a) for nonzero ξ . Significant improvements over direct imaging are still possible for small separations and $\xi \ll 1$.

For two-parameter estimation, consider the hybrid scheme in Fig. 6, assuming 50-50 beam-splitting and binary SPADE for example. For simplicity, assume that the binary-SPADE output is used only for separation estimation, such that the total information matrix with respect to θ_1 and θ_2 remains diagonal. Compared with direct imaging, the centroid information for the hybrid scheme is halved, viz.,

$$\mathcal{J}_{11}^{(\text{hybrid})} = \frac{\mathcal{J}_{11}^{(\text{direct})}}{2}, \quad (\text{F5})$$

but the separation information gained by binary SPADE can be appreciable, with

$$\mathcal{J}_{22}^{(\text{hybrid})} = \frac{\mathcal{J}_{22}^{(\text{direct})}}{2} + \frac{\mathcal{J}_{22}^{(\text{b})}}{2}. \quad (\text{F6})$$

The net performance of the hybrid scheme can be quantified in terms of the Cramér-Rao bounds for locating X_1 and X_2 . For a diagonal information matrix \mathcal{J} with respect to θ_1 and θ_2 , the bound on the mean-square error $\Sigma^{(X)}$ of estimating either $X_1 = \theta_1 - \theta_2/2$ or $X_2 = \theta_1 + \theta_2/2$ is simply

$$\Sigma_{ss}^{(X)} \geq \frac{1}{\mathcal{J}_{11}} + \frac{1}{4\mathcal{J}_{22}}, \quad s = 1, 2, \quad (\text{F7})$$

which demonstrates the detrimental effect of small \mathcal{J}_{22} for localization. Figure 8 compares the localization bounds for the hybrid scheme and direct imaging in log-log scale. For small separations, it can be seen that the increased separation information in the hybrid scheme more than compensates for the reduced centroid information and allows localization errors substantially lower than those for direct imaging. With a higher $N_1 = N/2$, more accurate centroid information from the imaging port can be used to reduce the misalignment at the SPADE port, and performance converging to the ideal $\xi = 0$ case in Fig. 8 can be expected for high N .

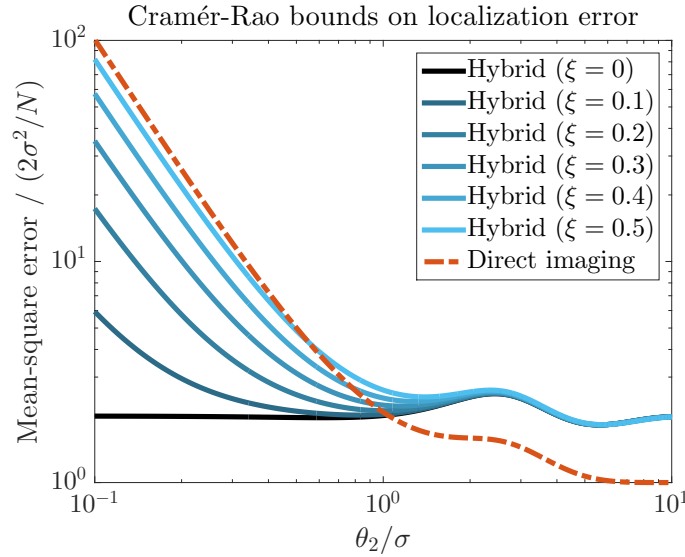


FIG. 8. Cramér-Rao bounds on the mean-square error of estimating X_1 or X_2 for a 50-50 hybrid scheme (solid) and direct imaging (dash-dotted). Note that the log-log scale is used here for clarity, unlike all the other plots. The vertical axis is normalized with respect to the error of locating an isolated source with direct imaging.

Appendix G: Monte Carlo analysis of SPADE with maximum-likelihood estimation

To confirm that the classical Cramér-Rao bounds satisfactorily represent the actual performance of SPADE for finite photon numbers, we simulate the device output data numerically, apply maximum-likelihood estimation, and investigate the resulting errors.

To refine our error analysis, we condition our results on the total number of detected photons L , which is obtained after an experiment, rather than the average photon number N [7]. It is not difficult to show that, conditioned on L , the classical and quantum Fisher information retain their expressions except that N is replaced by L . The error bounds become

$$\frac{1}{\mathcal{J}_{22}^{(\text{HG})}} \approx \frac{1}{\mathcal{K}'_{22}} \approx \frac{4\sigma^2}{L}. \quad (\text{G1})$$

It can also be shown that the sufficient statistic $\sum_q qm_q$ in the maximum-likelihood estimator for SPADE in Eq. (D7) is Poisson with mean LQ , so it is simple to generate samples of the maximum-likelihood estimates \check{Q}_{ML} and $\check{\theta}_{2\text{ML}}$ according to Eq. (D7).

Figure 9(a) plots the simulated mean-square errors, normalized with respect to Eq. (G1), for several values of L . It is intriguing to see that, as $\theta_2/\sigma \rightarrow 0$, the errors go below the bounds. This super-efficiency is a well known statistical phenomenon, as the maximum-likelihood estimation of θ_2 is actually biased for finite samples, and the simple Cramér-Rao bounds considered here need not apply.

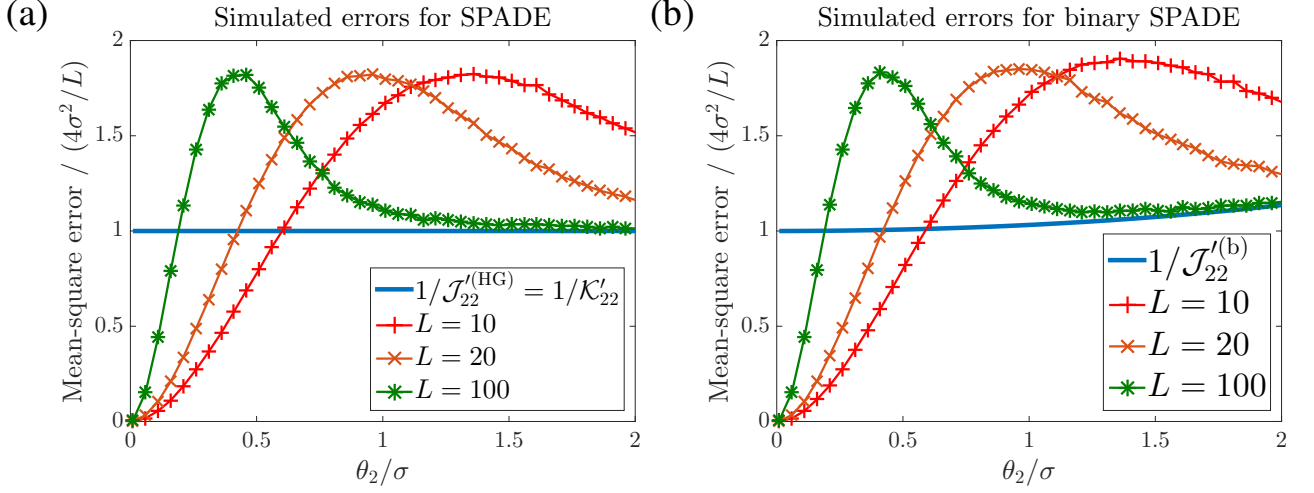


FIG. 9. Simulated mean-square errors for (a) SPADE and (b) binary SPADE with maximum-likelihood estimation, conditioned on L detected photons. Note that the vertical axis is normalized with respect to $4\sigma^2/L$, so the plotted values are the actual errors magnified by $L/(4\sigma^2)$. Each error is computed by averaging 10^5 simulations, and the lines connecting the data points are guides for eyes.

To analyze biased estimators, a better way is to use Bayesian bounds [9, 14], which apply to the global estimation error of any biased or unbiased estimator. A global error is obtained by averaging the frequentist error considered here over a prior distribution of θ_2 . With the constant Fisher information quantities in Eq. (G1), the Bayesian bounds are equal to their frequentist counterparts in the limit of negligible prior information. The limited rise and fall of the errors shown in Fig. 9(a) suggest that the global errors should remain close to the Bayesian bounds.

For our purpose, the main point of Fig. 9(a) is that the errors remain less than twice the Cramér-Rao bounds at worst and even offer the pleasant surprise of super-efficiency for small separations, thus supporting our use of the Fisher information measures to represent the performance of SPADE. The vanishing information for direct imaging for small separations, on the other hand, implies that its Bayesian version will suffer similarly when the prior distribution of θ_2 is concentrated at small θ_2/σ , and any estimator, biased or unbiased, cannot violate the Bayesian bound and must suffer as well.

For binary SPADE, the Fisher information conditioned on L has the same form as Eq. (E3), and the Cramér-Rao bound can be expressed as

$$\frac{1}{\mathcal{J}'_{22}^{(b)}} \approx \frac{4\sigma^2}{L} \frac{1 - \exp(-Q)}{Q \exp(-Q)}. \quad (\text{G2})$$

The sufficient statistic m_0 in $\tilde{\theta}_{2\text{ML}}^{(b)}$ given by Eq. (E4) is binomial and also simple to generate. In case $m_0 = 0$, we set $\tilde{\theta}_2 = 2\sigma$, the maximum of our considered range of θ_2 . Figure 9(b) plots the simulated mean-square errors for binary SPADE with otherwise the same parameters as those for Fig. 9(a). For small θ_2/σ , the errors follow very similar trends as their counterparts in Fig. 9(a), and for larger θ_2/σ the errors begin to follow the rising Cramér-Rao bound according to Eq. (G2), especially for $L = 100$. This supports our use of the Fisher information to represent the performance of binary SPADE.

To investigate the effect of misalignment, Fig. 10 plots the simulated errors for binary SPADE with a given misalignment level $\xi = 0.1$. The required overhead $N_1 \sim 100$ is negligible if $L \gg N_1$. Since ξ is unknown in reality, the maximum-likelihood estimator used in the simulations assumes zero misalignment for simplicity. Despite the model mismatch, the errors remain close to the Cramér-Rao bound, especially for larger L , and substantially below the bound for direct imaging.

For a given N , L has a mean $M\epsilon = N$ and standard deviation $\sqrt{M\epsilon(1-\epsilon)} \approx \sqrt{N}$. This means that the distribution of L becomes increasingly sharp around the mean at $L = N$ for large N , and we can expect the performance for a given $L = N$ to be an increasingly accurate approximation of the average performance in the constant- N , random- L scenario.

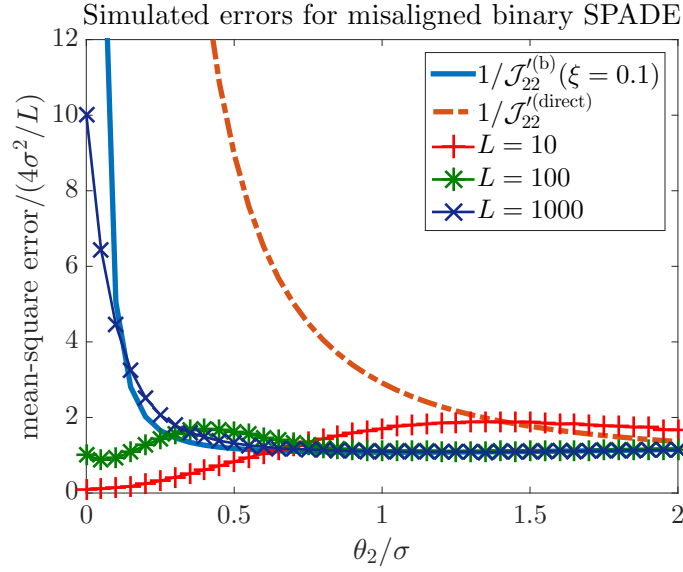


FIG. 10. Simulated mean-square errors of binary SPADE with misalignment level $\xi = 0.1$, conditioned on L detected photons. The maximum-likelihood estimator that assumes no misalignment is used. Note that the vertical axis is normalized with respect to $4\sigma^2/L$. Each error is computed by averaging 10^5 simulations, and the lines connecting the data points are guides for eyes. The errors are substantially below the Cramér-Rao bound for direct imaging (dash-dotted curve).

Appendix H: Other point-spread functions

Our analysis of SPADE so far relies on the assumption of a Gaussian point-spread function. For other point-spread functions, it is nontrivial to find a suitable basis of spatial modes, although we can still rely on the mathematical existence of a quantum-optimal measurement [17, 18] to be sure that the QCRB can be saturated. For a more concrete method, the analysis of the binary SPADE schemes is fortunately still tractable, if we assume a single-mode waveguide with a mode profile that matches the point-spread function $\psi(x)$ centered at the centroid position. Consider $\xi = 0$ for simplicity and define $|\psi\rangle = \int_{-\infty}^{\infty} dx \psi(x) |x\rangle$ as the state of one photon in the waveguide mode. The efficiency of coupling a photon in state $|\psi_1\rangle$ or $|\psi_2\rangle$ into the waveguide mode becomes

$$|\langle\psi|\psi_1\rangle|^2 = |\langle\psi|\psi_2\rangle|^2 = \left| \int_{-\infty}^{\infty} dx \psi^*(x) \psi\left(x + \frac{\theta_2}{2}\right) \right|^2 = \left| \int_{-\infty}^{\infty} dk |\Psi(k)|^2 \exp\left(\frac{ik\theta_2}{2}\right) \right|^2 \equiv \Upsilon(\theta_2), \quad (\text{H1})$$

where $\Upsilon(\theta_2)$ is the mode overlap factor and $\Psi(k) \equiv (2\pi)^{-1/2} \int_{-\infty}^{\infty} dx \psi(x) \exp(-ikx)$ is the optical transfer function of the imaging system before the image plane [32]. For the density operator in Eqs. (B9) and (B15), and (B16), or in fact any mixture of $|\psi_1\rangle\langle\psi_1|$ and $|\psi_2\rangle\langle\psi_2|$, the probability of finding a photon in the waveguide mode becomes $P(\psi) \approx \epsilon\Upsilon$, and the probability of finding a photon in any other mode is $P(\psi) \approx \epsilon(1 - \Upsilon)$. The Fisher information over M intervals is then

$$\mathcal{J}_{22}^{(b)} \approx \frac{N}{\Upsilon(1 - \Upsilon)} \left(\frac{\partial \Upsilon}{\partial \theta_2} \right)^2. \quad (\text{H2})$$

To study its behavior for small θ_2 , expand $\Upsilon(\theta_2)$ in Eq. (H1) as $\Upsilon(\theta_2) = 1 - \Delta k^2 \theta_2^2/4 + O(\theta_2^4)$ with $\Delta k^2 = \int_{-\infty}^{\infty} dk |\Psi(k)|^2 k^2 - [\int_{-\infty}^{\infty} dk |\Psi(k)|^2 k]^2$, giving

$$\mathcal{J}_{22}^{(b)}(\theta_2 = 0) \approx N \Delta k^2. \quad (\text{H3})$$

$\mathcal{J}_{22}^{(b)}$ can hence reach the quantum information $\mathcal{K}_{22} \approx N \Delta k^2$ at $\theta_2 = 0$, precisely where $\mathcal{J}_{22}^{(\text{direct})}$ vanishes and Rayleigh's curse is at its worst. For larger θ_2 , $\mathcal{J}_{22}^{(b)}$ is expected to decrease, as the scheme is unable to discriminate the higher-order modes that become more likely to be occupied. Figure 11 plots \mathcal{K}_{22} , the numerically computed $\mathcal{J}_{22}^{(\text{direct})}$, and $\mathcal{J}_{22}^{(b)}$ for the sinc point-spread function [1] $\psi(x) = (1/\sqrt{W}) \text{sinc}(x/W)$, where $W = \lambda/(2\text{NA})$, $\text{sinc } u \equiv \sin(\pi u)/(\pi u)$ for $u \neq 0$ and $\text{sinc}(0) \equiv 1$. The information quantities demonstrate behaviors similar to the Gaussian case.

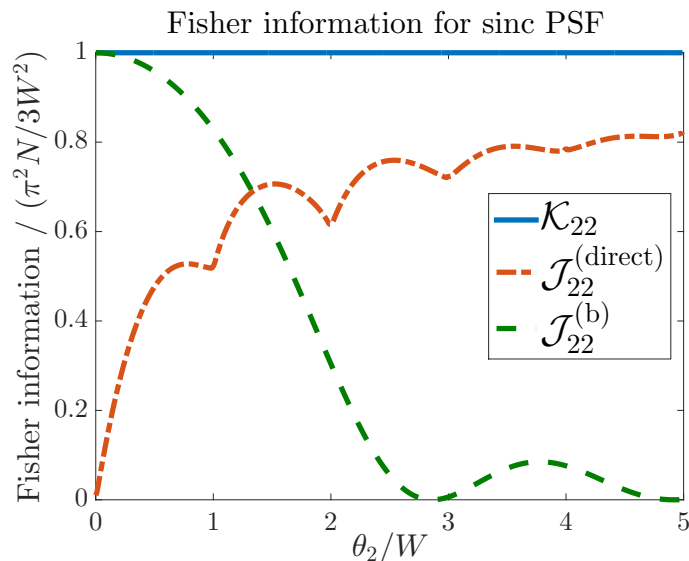


FIG. 11. Fisher information for separation estimation versus normalized separation θ_2/W for the sinc point-spread function. \mathcal{K}_{22} is the quantum value, $\mathcal{J}_{22}^{(\text{direct})}$ is the numerically computed value for direct imaging, and $\mathcal{J}_{22}^{(b)}$ is that for binary SPADE tailored for the sinc function. The vertical axis is normalized with respect to $\mathcal{K}_{22} = \pi^2 N / (3W^2)$.

Appendix I: Two-dimensional imaging

The essential physics remains unchanged when we consider two-dimensional imaging, and we discuss the generalization only briefly here; the details are given elsewhere [37, 39]. The single-photon state in Eq. (B15) should now be expressed as $|\psi_s\rangle = \int_{-\infty}^{\infty} dx \int_{-\infty}^{\infty} dy \psi_s(x, y) |x, y\rangle$, where $\langle x, y | x', y' \rangle = \delta(x - x') \delta(y - y')$ and $\psi_s(x, y)$ is a two-dimensional wavefunction [20]. In terms of a point-spread function $\psi(x, y)$ and unknown positions (X_1, Y_1) and (X_2, Y_2) , $\psi_s(x, y) = \psi(x - X_s, y - Y_s)$, and we can define the four centroid and separation parameters as $\theta_1 = (X_1 + X_2)/2$, $\theta_2 = X_2 - X_1$, $\theta_3 = (Y_1 + Y_2)/2$, and $\theta_4 = Y_2 - Y_1$. $\mathcal{J}^{(\text{direct})}$ for the estimation of θ_2 and θ_4 decreases to zero when the sources are close, and Rayleigh's curse still exists for direct imaging [8, 71]. On the other hand, the quantum Fisher information matrix, to be reported in Ref. [37], shows no sign of Rayleigh's curse for two-dimensional separation estimation.

For SPADE, we can use the two-dimensional Hermite-Gaussian basis [33]. Assuming a Gaussian point-spread function and a known centroid, it is straightforward to show that a measurement of each photon in the Hermite-Gaussian basis with mode indices q and p obeys a two-variable Poisson distribution, and the classical Fisher information with respect to θ_2 and θ_4 remains a constant and free of Rayleigh's curse, similar to the one-dimensional case. For other point-spread functions, such as the Airy disk [32, 72], binary SPADE with a matching mode profile can estimate the separation without Rayleigh's curse for small separations in the same way as the one-dimensional case, but information about the direction of the separation is lost. To obtain directional information, one needs to discriminate at least some of the higher-order modes in different directions.

A quadratic-index optical fiber can support two-dimensional Hermite-Gaussian modes, while a weakly guiding step-index fiber also has modes closely resembling the Hermite-Gaussian modes [34]. A complication arises for cylindrically symmetric fibers, as modes with the same total order $q + p$ will have a degenerate propagation constant, causing multiple modes to satisfy the same phase-matching conditions in grating or evanescent coupling and preventing discrimination of modes with the same order. The net result is that directional information is compromised. One solution is to turn the point-spread function into an elliptic one with asymmetric widths and use an elliptic fiber to break the degeneracy. A vectorial version of SLIVER [39] can work almost as well and will be reported in Ref. [37].

[1] Lord Rayleigh, "XXXI. Investigations in optics, with special reference to the spectroscope," *Philosophical Magazine Series* **5** *8*, 261–274 (1879).

[2] Stefan W. Hell and Jan Wichmann, "Breaking the diffraction resolution limit by stimulated emission: stimulated-emission-depletion fluorescence microscopy," *Opt. Lett.* **19**, 780–782 (1994).

- [3] Eric Betzig, “Proposed method for molecular optical imaging,” *Opt. Lett.* **20**, 237–239 (1995).
- [4] Stefan W. Hell, “Far-field optical nanoscopy,” *Science* **316**, 1153–1158 (2007).
- [5] Eric Betzig, George H. Patterson, Rachid Sougrat, O. Wolf Lindwasser, Scott Olenych, Juan S. Bonifacino, Michael W. Davidson, Jennifer Lippincott-Schwartz, and Harald F. Hess, “Imaging intracellular fluorescent proteins at nanometer resolution,” *Science* **313**, 1642–1645 (2006).
- [6] William E. Moerner, “New directions in single-molecule imaging and analysis,” *Proceedings of the National Academy of Sciences* **104**, 12596–12602 (2007).
- [7] E. Bettens, D. Van Dyck, A. J. den Dekker, J. Sijbers, and A. van den Bos, “Model-based two-object resolution from observations having counting statistics,” *Ultramicroscopy* **77**, 37–48 (1999).
- [8] Sripad Ram, E. Sally Ward, and Raimund J. Ober, “Beyond Rayleigh’s criterion: A resolution measure with application to single-molecule microscopy,” *Proceedings of the National Academy of Sciences of the United States of America* **103**, 4457–4462 (2006).
- [9] Harry L. Van Trees, *Detection, Estimation, and Modulation Theory, Part I*. (John Wiley & Sons, New York, 2001).
- [10] James B. Pawley, ed., *Handbook of Biological Confocal Microscopy* (Springer, New York, 2006).
- [11] Steve B. Howell, *Handbook of CCD Astronomy* (Cambridge University Press, Cambridge, 2006).
- [12] Jonas Zmuidzinas, “Cramér–Rao sensitivity limits for astronomical instruments: implications for interferometer design,” *J. Opt. Soc. Am. A* **20**, 218–233 (2003).
- [13] Antoine Labeyrie, Stephen G. Lipson, and Peter Nisenson, *An Introduction to Optical Stellar Interferometry* (Cambridge University Press, Cambridge, 2006).
- [14] Carl W. Helstrom, *Quantum Detection and Estimation Theory* (Academic Press, New York, 1976).
- [15] Vittorio Giovannetti, Seth Lloyd, and Lorenzo Maccone, “Advances in quantum metrology,” *Nature Photon.* **5**, 222–229 (2011).
- [16] Mankei Tsang, “Quantum limits to optical point-source localization,” *Optica* **2**, 646–653 (2015).
- [17] Masahito Hayashi, ed., *Asymptotic Theory of Quantum Statistical Inference: Selected Papers* (World Scientific, Singapore, 2005).
- [18] Akio Fujiwara, “Strong consistency and asymptotic efficiency for adaptive quantum estimation problems,” *Journal of Physics A: Mathematical and General* **39**, 12489 (2006).
- [19] Carl W. Helstrom, “Resolution of point sources of light as analyzed by quantum detection theory,” *IEEE Transactions on Information Theory* **19**, 389–398 (1973).
- [20] Horace P. Yuen and Jeffrey H. Shapiro, “Optical communication with two-photon coherent states—Part I: Quantum-state propagation and quantum-noise,” *IEEE Transactions on Information Theory* **24**, 657–668 (1978).
- [21] Mikhail I. Kolobov, “The spatial behavior of nonclassical light,” *Rev. Mod. Phys.* **71**, 1539–1589 (1999).
- [22] L. A. Lugiato, A. Gatti, and E. Brambilla, “Quantum imaging,” *Journal of Optics B: Quantum and Semiclassical Optics* **4**, S176 (2002).
- [23] Yanhua Shih, “Quantum imaging,” *IEEE Journal of Selected Topics in Quantum Electronics* **13**, 1016–1030 (2007).
- [24] Baris I. Erkmen and Jeffrey H. Shapiro, “Ghost imaging: from quantum to classical to computational,” *Adv. Opt. Photon.* **2**, 405–450 (2010).
- [25] Philip R. Hemmer and Todd Zapata, “The universal scaling laws that determine the achievable resolution in different schemes for super-resolution imaging,” *Journal of Optics* **14**, 083002 (2012).
- [26] Joseph W. Goodman, *Statistical Optics* (Wiley, New York, 1985).
- [27] Leonard Mandel and Emil Wolf, *Optical Coherence and Quantum Optics* (Cambridge University Press, Cambridge, 1995).
- [28] Raimund J. Ober, Sripad Ram, and E. Sally Ward, “Localization accuracy in single-molecule microscopy,” *Biophysical Journal* **86**, 1185–1200 (2004).
- [29] Mankei Tsang, “Quantum nonlocality in weak-thermal-light interferometry,” *Phys. Rev. Lett.* **107**, 270402 (2011).
- [30] Ivan R. King, “Accuracy of measurement of star images on a pixel array,” *Publications of the Astronomical Society of the Pacific* **95**, 163–168 (1983).
- [31] Hendrik Deschout, Francesca Cella Zancchi, Michael Mlodzianoski, Alberto Diaspro, Joerg Bewersdorf, Samuel T Hess, and Kevin Braeckmans, “Precisely and accurately localizing single emitters in fluorescence microscopy,” *Nature Methods* **11**, 253–266 (2014).
- [32] Joseph W. Goodman, *Introduction to Fourier Optics* (McGraw-Hill, New York, 2004).
- [33] Amnon Yariv, *Quantum Electronics* (Wiley, New York, 1989).
- [34] Amnon Yariv and Pochi Yeh, *Photonics: Optical Electronics in Modern Communications* (Oxford University Press, New York, 2007).
- [35] W. V. Sorin, B. Y. Kim, and H. J. Shaw, “Highly selective evanescent modal filter for two-mode optical fibers,” *Opt. Lett.* **11**, 581–583 (1986).
- [36] Mankei Tsang, Ranjith Nair, and Xiao-Ming Lu, “Semiclassical Theory of Superresolution for Two Incoherent Optical Point Sources,” ArXiv e-prints (2016), [arXiv:1602.04655 \[quant-ph\]](https://arxiv.org/abs/1602.04655).
- [37] Shan Zheng Ang, Ranjith Nair, and Mankei Tsang, Under preparation.
- [38] Ranjith Nair and Mankei Tsang, “Ultimate quantum limit on resolution of two thermal point sources,” ArXiv e-prints (2016), [arXiv:1604.00937 \[quant-ph\]](https://arxiv.org/abs/1604.00937).
- [39] Ranjith Nair and Mankei Tsang, “Interferometric superlocalization of two incoherent optical point sources,” *Opt. Express* **24**, 3684–3701 (2016).
- [40] Ranjith Nair and Mankei Tsang, Under preparation.
- [41] Carl W. Helstrom, “Estimation of object parameters by a quantum-limited optical system,” *J. Opt. Soc. Am.* **60**, 233–239 (1970).
- [42] Lennart Lindgren, “Photoelectric astrometry - A comparison of methods for precise image location,” in *IAU Colloq. 48: Modern Astrometry*, edited by F. V. Prochazka and R. H. Tucker (1978) pp. 197–217.
- [43] Norman Bobroff, “Position measurement with a resolution and noise-limited instrument,” *Review of Scientific Instruments* **57**, 1152–1157 (1986).
- [44] V. Delaubert, N. Treps, C. Fabre, H. A. Bachor, and P. Réfrégier, “Quantum limits in image processing,” *EPL (Europhysics Letters)* **81**, 44001 (2008).
- [45] Ranjith Nair and Brent J. Yen, “Optimal quantum states for image sensing in loss,” *Phys. Rev. Lett.* **107**, 193602 (2011).
- [46] Carlos A. Pérez-Delgado, Mark E. Pearce, and Pieter Kok, “Fundamental limits of classical and quantum imaging,” *Phys. Rev. Lett.* **109**, 123601 (2012).
- [47] C. Fabre, J. B. Fouet, and A. Maître, “Quantum limits in the measurement of very small displacements in optical images,” *Optics Letters* **25**, 76–78 (2000).

- [48] S. M. Barnett, C. Fabre, and A. Maître, “Ultimate quantum limits for resolution of beam displacements,” *The European Physical Journal D - Atomic, Molecular, Optical and Plasma Physics* **22**, 513–519 (2003).
- [49] Nicolas Treps, Nicolai Grosse, Warwick P. Bowen, Claude Fabre, Hans-A. Bachor, and Ping Koy Lam, “A quantum laser pointer,” *Science* **301**, 940–943 (2003).
- [50] Michael A. Taylor, Jiri Janousek, Vincent Daria, Joachim Knittel, Boris Hage, Hans-A. Bachor, and Warwick P. Bowen, “Biological measurement beyond the quantum limit,” *Nature Photonics* **7**, 229–233 (2013).
- [51] Mikhail I. Kolobov, ed., *Quantum Imaging* (Springer, New York, 2007).
- [52] Mikhail I. Kolobov and Claude Fabre, “Quantum limits on optical resolution,” *Phys. Rev. Lett.* **85**, 3789–3792 (2000).
- [53] Vladislav N. Beskrovnyy and Mikhail I. Kolobov, “Quantum limits of super-resolution in reconstruction of optical objects,” *Phys. Rev. A* **71**, 043802 (2005).
- [54] Vladislav N. Beskrovnyy and Mikhail I. Kolobov, “Quantum-statistical analysis of superresolution for optical systems with circular symmetry,” *Phys. Rev. A* **78**, 043824 (2008).
- [55] Kevin Piché, Jonathan Leach, Allan S. Johnson, Jeff Z. Salvail, Mikhail I. Kolobov, and Robert W. Boyd, “Experimental realization of optical eigenmode super-resolution,” *Opt. Express* **20**, 26424–26433 (2012).
- [56] Vittorio Giovannetti, Seth Lloyd, Lorenzo Maccone, and Jeffrey H. Shapiro, “Sub-Rayleigh-diffraction-bound quantum imaging,” *Phys. Rev. A* **79**, 013827 (2009).
- [57] Mankei Tsang, “Quantum imaging beyond the diffraction limit by optical centroid measurements,” *Phys. Rev. Lett.* **102**, 253601 (2009).
- [58] Heedeuk Shin, Kam Wai Clifford Chan, Hye Jeong Chang, and Robert W. Boyd, “Quantum spatial superresolution by optical centroid measurements,” *Phys. Rev. Lett.* **107**, 083603 (2011).
- [59] Lee A. Rozema, James D. Bateman, Dylan H. Mahler, Ryo Okamoto, Amir Feizpour, Alex Hayat, and Aephraim M. Steinberg, “Scalable spatial superresolution using entangled photons,” *Phys. Rev. Lett.* **112**, 223602 (2014).
- [60] S. Oppel, T. Büttner, P. Kok, and J. von Zanthier, “Superresolving multiphoton interferences with independent light sources,” *Phys. Rev. Lett.* **109**, 233603 (2012).
- [61] Osip Schwartz, Jonathan M. Levitt, Ron Tenne, Stella Itzhakov, Zvicka Deutsch, and Dan Oron, “Superresolution microscopy with quantum emitters,” *Nano Letters* **13**, 5832–5836 (2013).
- [62] Jin-Ming Cui, Fang-Wen Sun, Xiang-Dong Chen, Zhao-Jun Gong, and Guang-Can Guo, “Quantum statistical imaging of particles without restriction of the diffraction limit,” *Phys. Rev. Lett.* **110**, 153901 (2013).
- [63] D. Gatto Monticone, K. Katamadze, P. Traina, E. Moreva, J. Forneris, I. Ruo-Berchera, P. Olivero, I. P. Degiovanni, G. Brida, and M. Genovese, “Beating the abbe diffraction limit in confocal microscopy via nonclassical photon statistics,” *Phys. Rev. Lett.* **113**, 143602 (2014).
- [64] Agedi N. Boto, Pieter Kok, Daniel S. Abrams, Samuel L. Braunstein, Colin P. Williams, and Jonathan P. Dowling, “Quantum interferometric optical lithography: Exploiting entanglement to beat the diffraction limit,” *Phys. Rev. Lett.* **85**, 2733–2736 (2000).
- [65] Robert W. Boyd and Jonathan P. Dowling, “Quantum lithography: status of the field,” *Quantum Information Processing* **11**, 891–901 (2012).
- [66] T. B. Pittman, Y. H. Shih, D. V. Strekalov, and A. V. Sergienko, “Optical imaging by means of two-photon quantum entanglement,” *Phys. Rev. A* **52**, R3429–R3432 (1995).
- [67] A. Gatti, E. Brambilla, M. Bache, and L. A. Lugiato, “Ghost imaging with thermal light: Comparing entanglement and classical correlation,” *Phys. Rev. Lett.* **93**, 093602 (2004).
- [68] Daniel Gottesman, Thomas Jennewein, and Sarah Croke, “Longer-baseline telescopes using quantum repeaters,” *Phys. Rev. Lett.* **109**, 070503 (2012).
- [69] Larry A. Wasserman, *All of Statistics* (Springer, New York, 2004).
- [70] Howard M. Wiseman and Gerard J. Milburn, *Quantum Measurement and Control* (Cambridge University Press, Cambridge, 2010).
- [71] S. Van Aert, A. J. den Dekker, D. Van Dyck, and A. van den Bos, “High-resolution electron microscopy and electron tomography: resolution versus precision,” *Journal of Structural Biology* **138**, 21–33 (2002).
- [72] Max Born and Emil Wolf, *Principles of Optics: Electromagnetic Theory of Propagation, Interference and Diffraction of Light* (Cambridge University Press, Cambridge, 1999).